ISSN 1063-7834, Physics of the Solid State, 2019, Vol. 61, No. 11, pp. 1960–1968. © Pleiades Publishing, Ltd., 2019.
Russian Text © The Author(s), 2019, published in Fizika Tverdogo Tela, 2019, Vol. 61, No. 11, pp. 2000–2008.

METALS

Finding a New *B*1-Type Phase in Single Crystals of Fe–Al and Fe–Ga Soft Magnetic Alloys

Yu. P. Chernenkov[a], N. V. Ershov[b, *], and V. A. Lukshina[b, c]

[a] *Petersburg Nuclear Physics Institute, Nuclear Research Center "Kurchatov Institute", Gatchina, Leningrad oblast, 188350 Russia*

[b] *Mikheev Institute of Metal Physics, Ural Branch, Russian Academy of Sciences, Yekaterinburg, 620180 Russia*

[c] *Ural Federal University Named after the First President of Russia B.N. Yeltsin, Yekaterinburg, 620002 Russia*

**e-mail: nershov@imp.uran.ru*

Received June 19, 2019; revised June 19, 2019; accepted June 24, 2019

Abstract—The atomic structure of Fe–Al (7 and 9 at % Al) and Fe–Ga (18 at % Ga) alloys is studied by X-ray diffraction using a laboratory four-circle diffractometer. After refining annealing, single-crystal alloy samples were annealed in the ferromagnetic state ($T < T_C$). One sample of the Fe–18 at % Ga alloy, after short holding in the paramagnetic state ($T > T_C$), was quenched in room temperature water. Earlier, the authors reported on the peculiarities of the ordering of alloying atoms in $B2$ and $D0_3$ phase structures in quenched and annealed samples of these alloys. Here, we present and discuss the results of our observations in these alloys of a new phase with a face-centered cubic (fcc) lattice ($B1$-type structure with NaCl prototype and unit cell parameter ~5.2 nm). The fcc phase appears in the Fe–Al alloy as the aluminum concentration increases from 7 to 9 at %; it is observed in the Fe–18 at % Ga alloy, and its volume fraction increases after annealing in the ferromagnetic state in comparison with a quenched alloy sample. In these alloys (9 at % Al) and (18 at % Ga), different ways of embedding fcc crystals in the bcc phase of single crystals are realized; i.e., the axes of the fcc lattice are directed in four different ways relative to the axes of the bcc lattice.

Keywords: soft magnetic materials, iron–aluminum and iron–gallium alloys, X-ray diffraction, atomic structure, new $B1$-type phase, heat treatment

DOI: 10.1134/S1063783419110118

1. INTRODUCTION

In recent years, interest in Fe–Al and Fe–Ga alloys has intensified again, since they possess technological properties important for practical applications [1]. Iron–aluminum alloys are resistant to oxidation and corrosion, have good ductility at room temperature, relatively low density, high magnetic permeability, and absorb mechanical vibration well. Iron-rich alloys of iron and gallium became objects of considerable scientific and practical interest after Clark et al. [2] reported the discovery of more than a ten-fold increase in magnetostriction due to the addition of gallium to iron, the maximum of which is observed at a gallium concentration of about 17 at %.

In the α-region of the phase diagram [3], i.e., in the region of disordered solid solution ($A2$ structure), Fe–Al alloys (up to 20 at % Al) are magnetically soft and possess features important for their practical application, which are caused by the structural state of the alloys: induced magnetic anisotropy that occurs after thermomagnetic or thermomechanical treatment; quadratic dependence of the tetragonal magnetostriction coefficient on aluminum concentration; and unusual behavior of electrical resistance as a function of temperature, the so-called K-state. According to the phase diagram of Fe–Ga alloys [4], at alloying element concentrations up to 18 at % and temperatures exceeding 750°C, the alloys are in the paramagnetic state and their structure is a disordered solid solution of gallium in α-iron ($A2$). As the temperature decreases, they transform into the ferromagnetic state and the two-phase region, where the $A2$ phase coexists with the second phase, Fe_3Ga, with a $D0_3$-type structure.

Studies of local ordering in Fe–Si alloys showed [5–7] that, in quenched samples of the alloy containing 5–10 at % Si, there are clusters with a $B2$-type order. With an increase in the Si concentration from 6 to 8 at %, small regions with the $D0_3$ order appear, the sizes and volume fraction of which increase after 10 min holding at a temperature of 450°C. At 10 at % silicon, the $D0_3$ phase is realized in the form of regions with long-range ordering [7]. $B2$-clusters consist of a "core" consisting of two $B2$-cells (CsCl-type order) with a common face, surrounded by stretched α-iron cells. $B2$-clusters have an anisotropic form: they are

more extended along one of the easy magnetization axes, ⟨100⟩. Regions with local $B2$ ordering coexisting with small clusters of the $D0_3$-phase were also found in single crystals of the Fe–Al alloy with 7 at % Al [8]. These results were obtained from X-ray diffraction data after analyzing the angular distribution of the intensity of weak, but very informative diffuse scattering.

X-ray diffraction studies of the atomic structure of single crystals of the Fe–Ga alloy with a Ga content of about 18 at % showed [9] that, in the alloy samples, Ga atoms are ordered and the size of the regions and the type of ordering in them depend on the conditions of heat treatment of the alloy. In the diffraction patterns of the sample quenched in water after holding in the paramagnetic state, besides strong peaks from the main body-centered cubic (bcc) structure, superstructure peaks are visible. They are due to scattering not only by the $B2$ and $D0_3$ regions, but also by regions of the new, observed for the first time, phase with a face centered cubic (fcc) lattice (cell parameter ~0.52 nm). Annealing in the ferromagnetic state does not lead to a noticeable change in the contribution to the scattering by small (subnanoscale, ~0.6 nm) $B2$-phase clusters, while the $D0_3$-peaks become narrower and their intensity increases by almost two orders of magnitude. It should be noted that the fcc phase was observed earlier, e.g., in [10], but its lattice parameter was ~0.367 nm and the structure was of the $AuCu_3$ type. It is noteworthy that the diagonal length of the face of the unit cell where the Fe–Ga–Fe atoms are located is $0.367 \times \sqrt{2} \approx 0.52$ nm, i.e., equal to the edge of the unit cell of the new fcc phase with the same atomic sequence (Fe–Ga–Fe). In [11], in the diffraction pattern of a single crystal of the Fe–18.7 at % Ga alloy, shown in Fig. 9, two peaks are seen whose positions ([HHH] with $H = 0.64$ and 1.28) are in good agreement with those calculated for peaks (200) and (400) from the new fcc phase that we discovered, with a cell parameter of ~0.52 nm. However, the authors of [11] give no comment on these peaks.

The objectives of this study were to identify a face-centered cubic phase that is new for alloys of iron with aluminum and gallium, as well as to determine the mean size of regions with an fcc phase.

2. EXPERIMENTAL

Structural studies were carried out on single-crystal samples of Fe–Al and Fe–Ga alloys and a pure Fe single crystal as a reference in X-ray diffraction measurements.

Single-crystal samples of Fe alloys with 7 at % Al and with 18 at % Ga were cut from a monolithic crystal grown by the Bridgeman method in the form of thin disks (thickness of 0.30–0.35 mm and diameter of 8–9 mm) with the Goss orientation of the crystallographic axes ({110}⟨001⟩). The sample plane is parallel to the crystallographic plane (110); one easy axis [001] lies in the disk plane, whereas the axes [100] and [010] make an angle of about 45° with the sample plane. Samples of Fe alloy with 9 at % Al were cut from macroscopic grain of a rolled sheet of electrical steel with a thickness of 0.35 mm, which also has a Goss orientation. All samples were subjected to preliminary refining annealing in a vacuum of $5–6 \times 10^{-6}$ mm Hg at a temperature of 1150–1300°C for 4 h. In addition, a single-crystal iron sample was prepared in the form of a thin plate with a plane close to the crystallographic plane (113). The carbon content in it did not exceed 0.06 wt %.

The intensity distribution of diffuse scattering along certain directions in the reciprocal lattice of a Fe single crystal is compared with a similar distribution for alloy samples in order to distinguish the contribution to them due to local ordering of impurity atoms, as well as to identify the contribution of diffuse planes and rods, characteristic of the bcc lattice, due to thermal motion of atoms [12].

After refining annealing, a sample of each alloy was annealed for one hour at a temperature $T_{an} = 450$°C, not exceeding the Curie point of the alloy ($T_C \sim 750$°C). The annealing temperature T_{an} is much lower than T_C, but sufficient to activate the diffusion of Al or Ga in Fe and to achieve an equilibrium state. The second sample of Fe alloy with 18 at % Ga was quenched in water (quenching rate of ~400°C/s) after ten-minute annealing at 850°C. It is assumed the state formed during annealing in the paramagnetic region ($T_{an} > T_C$) is thus fixed. After heat treatment, the thickness of the samples was brought to 40–50 μm using mechanical and chemical polishing. X-ray diffraction patterns were measured at room temperature on a four-circle laboratory diffractometer (Petersburg Nuclear Physics Institute, Research Nuclear Center Kurchatov Institute) in the transmission geometry [5]. The characteristic radiation of an X-ray tube with Mo anode ($\lambda = 0.071$ nm) was monochromatized using a pyrolytic graphite crystal. Scattered radiation was registered by a Si (Li) energy-dispersive detector, which significantly improved the signal/background ratio.

3. RESULTS AND DISCUSSION

X-ray diffraction patterns of the samples of Fe alloys with 7 at % Al and 18 at % Ga and the results of their detailed analysis were published in [8, 9]. In the article devoted to the effect of annealing in the ferromagnetic state on the structure of the Fe alloy with 18 at % Ga, the first indications are given of the presence in the diffraction patterns of a small contribution from the cubic face-centered phase (an NaCl-type structure), which has never been previously observed in soft magnetic Fe alloys with Al and Ga [3, 4].

In the phase diagrams of Fe alloys with Al or Ga, e.g., in [4], the following types of atomic ordering are observed: $A2$, bcc (prototype W); $B2$, bcc (prototype

CsCl); $L1_2$, fcc (prototype $AuCu_3$); $D0_3$, fcc (prototype BiF_3); and $D0_{19}$, close-packed hexagonal (cph) (prototype Ni_3Sn). According to international tables for diffraction crystallography, for these types of ordering, reflections with the following indices are allowed [13]. If n is an integer number ($n = 1, 2, 3, ...$), then, for $A2$ (space group $Im\bar{3}m$, no. 229) h, k, l: $h + k + l = 2n$; $0kl$: $k + l = 2n$; hhl: $l = 2n$; $h00$: $h = 2n$. For the $B2$ and $L1_2$ phases ($Pm\bar{3}m$, no. 221), any integer values of the indices h, k, and l are admissible. In the case of the $D0_3$ phase ($Fm\bar{3}m$, no. 225), hkl: $h + k$, $h + l$, $k + l = 2n$; $0kl$: k, $l = 2n$; hhl: $h + l = 2n$; $h00$: $h = 2n$, and the $D0_{19}$ phase, ($P6_3/mmc$, no. 194) hkl: $l = 2n$, $h - k = 3n + 1$, $h - k = 3n + 2$; hhl: $l = 2n$, $00l$: $l = 2n$. When the $D0_3$ phase is formed, the bcc cell is doubled along the three crystallographic axes $\langle 100 \rangle$. To simplify the description of X-ray diffraction patterns, peaks from the $D0_3$ phase will be indexed as reflections from the bcc lattice; i.e., some of them will contain half-integer indices.

In disordered iron alloys (phase $A2$), at low concentrations, the alloying elements (Si, Al, or Ga) occupy any position in the bcc lattice with equal probability. An ordered phase with a $B2$-type structure is present in the phase diagram at sufficiently high temperatures (>500°C) and concentrations (>20%) [3, 4, 14]. At low temperatures ($T \sim 20$°C) and low concentrations, it is observed in alloys in the form of regions with a size of ~0.6 nm [7–9]. The ordered $D0_3$-phase appears near the boundary of the two-phase region of the phase diagram (the $A2$ and $D0_3$ phases), while the mean size and volume fraction of the $D0_3$-phase regions strongly depend on the concentration and heat treatment conditions.

The main strong Bragg reflections from α-Fe–Al and α-Fe–Ga alloys (bcc lattice, phase $A2$) remain approximately the same as in the case of pure α-iron; i.e., the long-range order is preserved; but, in the diffraction patterns, they are shifted in the direction of smaller scattering angles, which is due to an increase in the bcc cell parameter upon dissolution of Al [15] or Ga [16]. The cell parameter a was determined from the angular positions of the Bragg peaks from the bcc lattice: in iron alloys with aluminum, $a = 0.2879(1)$ and 0.2883(1) nm, respectively, with 7 and 9 at % Al and $a = 0.2899(2)$ nm with 18 at % Ga (in α-iron, $a =$ 0.2866 nm).

If regions with $B2$ or $D0_3$ ordering in alloys are formed, superstructure peaks appear in the diffraction patterns for which $h + k + l = 2n + 1$ (forbidden for $A2$), i.e., peaks with indices (100), (300), (111), etc. In addition, upon the formation of the $D0_3$ phase, superstructure reflections with half-integer (for the bcc lattice) indices $h = n/2$, $k = m/2$, and $l = p/2$, where n, m, and p are odd numbers, e.g., (0.5 0.5 0.5), (1.5 0.5 0.5), (1.5 1.5 0.5), (1.5 1.5 1.5), etc., appear.

From the width of superstructure peaks, one can estimate the mean size of the regions with $B2$ and $D0_3$ ordering types. In the Fe–Al alloy at 7 at % Al, clusters with a mean size of 0.6–0.7 nm, containing pairs of Al atoms that are second nearest neighbors to each other, were detected [8]. In addition to $B2$-clusters, regions with local $D0_3$-type ordering arise, the mean size of which is about 0.6 nm, and corresponds to the parameter of one $D0_3$ unit cell. $D0_3$-regions with such a small mean size were detected for the first time due to the high sensitivity of the X-ray diffraction method.

In the Fe–Ga alloy samples, the ordering of Ga atoms also takes place [9]. The type of atomic ordering in the regions of the crystal and the size of the regions depend on the conditions of heat treatment of the alloy. In the diffraction patterns of the sample quenched in water after holding in the paramagnetic state, besides strong peaks from the main bcc structure, the contribution of diffuse scattering from the $B2$ and $D0_3$ phases and the fcc phase detected for the first time is also observed. Annealing in the ferromagnetic state does not lead to a noticeable change in the contribution to the scattering from small (~0.6 nm) $B2$-phase clusters, while the $D0_3$-peaks become narrow and their intensity increases by almost two orders of magnitude.

In order to distinguish in the X-ray diffraction patterns of samples of Fe alloys with Al and Ga the contribution due to scattering by regions with local $B2$- and $D0_3$-type ordering, as well as the contribution from the fcc phase, the figures below, in addition to the diffraction patterns of the alloys, contain the diffraction patterns of the sample of pure α-iron, for comparison. Figure 1 shows the angular distribution of scattering intensity upon scanning along the $\langle 100 \rangle$ axes of Fe–Al single crystals with 7 at % and 9 at % Al, measured between the (000)–(002) and (002)–(004) Bragg points of the reciprocal lattice. In comparison with the diffraction pattern of the Fe single crystal, the diffraction pattern of the alloy contains wide diffuse peaks, the maxima of which are shifted in the direction of smaller scattering angles from the positions calculated for (001) and (003). According to the results of the analysis of diffraction patterns given earlier in [8], the appearance of diffuse peaks is due to the local ordering of aluminum atoms in the bcc iron in the form of $B2$-phase clusters. In the diffraction patterns of the Fe–9 at % Al alloy, obtained by scanning along all three $\langle 100 \rangle$ directions, besides of diffuse peaks, reflections from a phase that was not previously observed in Fe–Al alloys are seen. In the text and figures below, reflexes of the new phase will be denoted as (hkl)-FCC. From their angular position and the regularity of extinction in diffraction patterns measured not only along the $\langle 100 \rangle$ axes (Fig. 1), but also along the [110] and [111] axes, as shown below in Figs. 3 and 5, respectively, it is possible to determine the type ($B1$, fcc, prototype NaCl) and the lattice

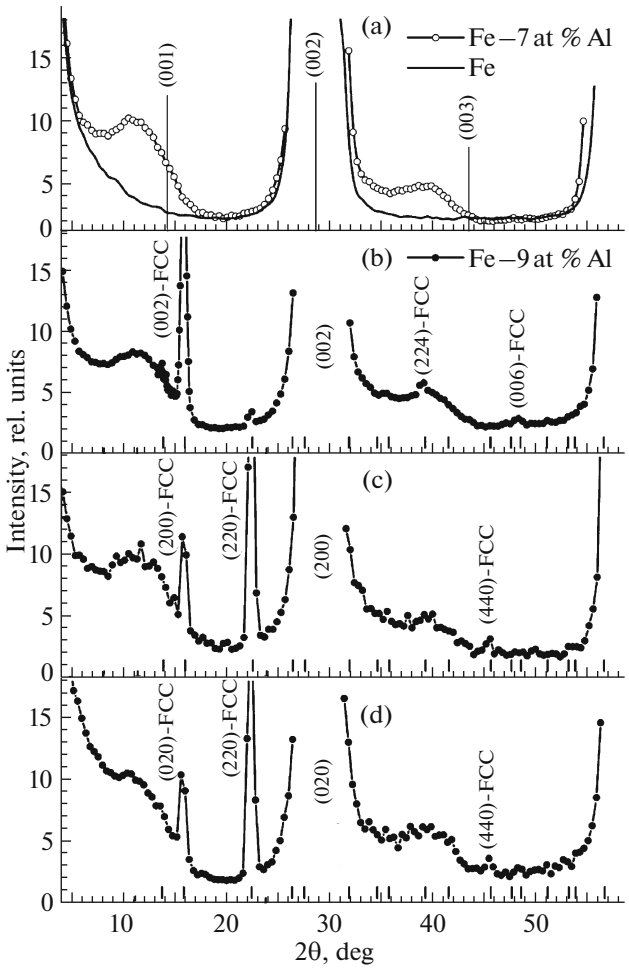

Fig. 1. Angular distribution of scattering intensity upon scanning along the ⟨100⟩ axes of single crystals of the Fe–Al alloy (7 at % Al) and (9 at % Al): (a, b) along the [001] axis, which lies in the sample plane, (c) along the [100] axis, and (d) along the [010] axis, which make an angle of about 45° with the sample plane; (a) the vertical lines indicate the reflection position (002) and calculated positions of the (001) and (003) peaks; (b–d) vertical strokes indicate the positions of the allowed peaks of the fcc phase.

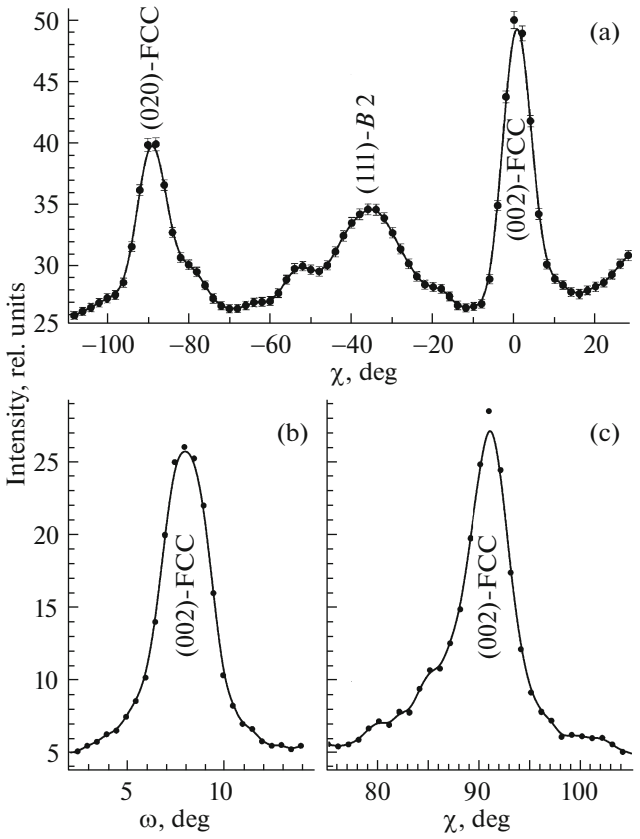

Fig. 2. Angular distribution of the scattering intensity from a single-crystal sample of the Fe–Al alloy (9 at % Al): (a) obtained by rotating it about the χ-axis, normal to the sample surface and passing through its center (the detector is at an angle of 2θ = 15.5°, the scattering vector lies in the sample plane); (b) by rotation about the ω-axis; and (c) by rotation about the χ-axis upon scanning through the (002)-FCC peak shown in Fig. 1b at 2θ = 15.8°.

parameter $a \sim 0.52$ nm. In Figs. 1b–1d, vertical strokes plotted along the abscissa axis show the calculated position of the reflections allowed for the fcc structure ($Fm\bar{3}m$). According to the Scherrer formula [17], from the peak width of the (002)-FCC in the diffraction pattern measured in θ–2θ scanning along the [002] axis, shown in Fig. 1b, the mean size of the fcc-phase regions is estimated by about 5 nm.

In the diffraction patterns shown in Figs. 1b–1d, in addition to the fcc peaks with indices of the {*h*00}-FCC type, e.g., (200)-FCC and (600)-FCC, there is a (220)-FCC peak. This means that FCC cells are embedded in a bcc lattice in more than one way. In other words, in addition to this way (which we called first and which is unlikely, as will be shown below) when the axes of the fcc cell coincide with the axes of the bcc lattice, there are others, in particular, when two ⟨110⟩-FCC-type axes coincide with the ⟨100⟩ axes of the bcc lattice. This second way has three variants of embedding (formally, 24, due to cubic symmetry). The different intensities of the {220}-FCC reflections in the diffraction patterns measured along different ⟨100⟩ axes of the bcc lattice may mean that the number of fcc nanocrystals—regions of the fcc phase in the alloy single crystal—is different, with one or another orientation of their axes relative to the axes of the bcc lattice, i.e., with one or another variant of embedding in it.

In principle it is not excluded that the axes of the fcc nanocrystals are randomly oriented relative to the axes of the bcc crystal. Then, the scattering by nanocrystals must be as by powder grains. The rotation of the sample around one or another axis must not lead to a change in the intensity of the observed fcc reflections, or, if there is a preferred orientation of the axes of nanocrystals, must lead to some its monotonic

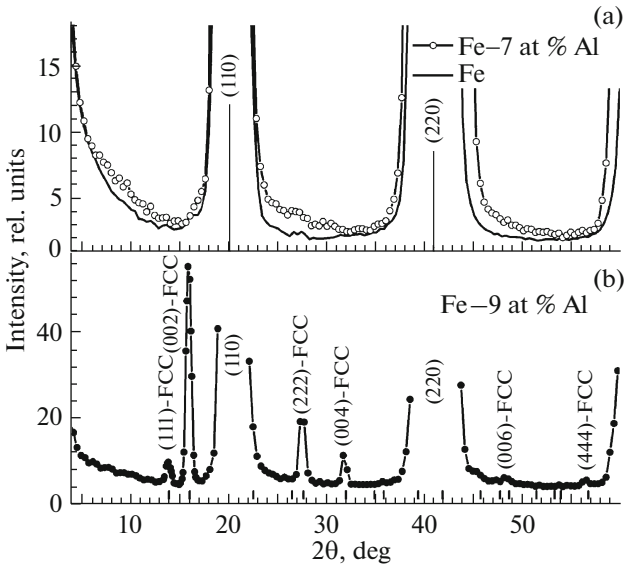

Fig. 3. Angular distribution of scattering intensity upon scanning along the [110] axis of (a) an α-iron single crystal and single crystals of Fe–Al alloys with (a) 7 at % Al and (b) 9 at % Al. The [110] axis lies in the plane of alloy samples. On the graph, (a) vertical lines indicate the positions of reflections (110) and (220) and (b) vertical strokes indicate the positions of the peaks of the fcc phase.

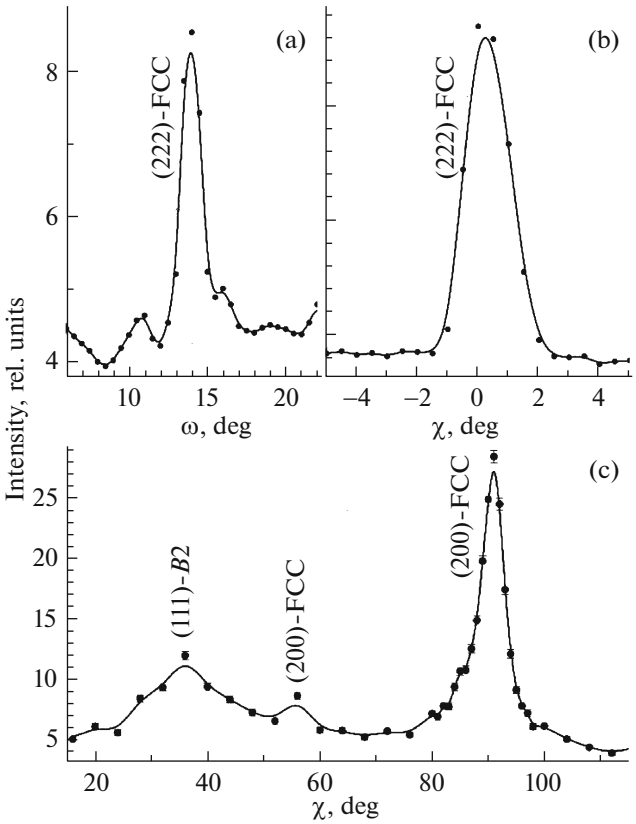

Fig. 4. Angular distribution of scattering intensity upon (a) ω- and (b) χ-scanning through the maximum of peak (222) at an angle of $2\theta = 27.4°$ in the diffraction pattern in Fig. 3b; (c) χ-scan in the $(\bar{1}\,10)$ plane of the bcc lattice at $2\theta = 15.8°$ (intersects the [001] axis at $\chi = 90°$ and the [111] axis of the bcc lattice at $\chi = 36°$). At the calculated angle $\chi = 55°$, a weak {200}-FCC peak is visible.

change. In order to verify the nature of the intensity distribution of fcc reflections, a diffraction pattern was measured upon rotation of the alloy sample with 9 at % Al by an angle χ about an axis coinciding with the axis $[1\,\bar{1}0]$ of the crystal, which is approximately perpendicular to the disk plane. The diffraction pattern is shown in Fig. 2a.

The fact that the (200)-FCC peak, which, in Fig. 1, is at an angle of $2\theta = 15.5°$, is visible both at $\chi = -90°$, when the axis is horizontal, i.e., in the scattering plane, and at $\chi = 0°$, when the [110] axis is horizontal, implies that the axes of fcc nanocrystals are oriented in the bcc lattice not randomly, but in accordance with one of the three variants of embedding fcc cells in the bcc crystal lattice. The wide diffuse peak with a maximum at an angle $\chi \sim -36°$ corresponds to the intersection of the scan path (circular arc) with the region of diffuse scattering by *B*2-clusters near the [111] axis in the reciprocal lattice of the bcc crystal, as shown below in the diffraction patterns measured upon scanning along the [111] axis and shown in Fig. 5.

Figures 2b and 2c show ω- and χ-scans through the maximum of the [002]-FCC peak for the Fe–Al alloy sample (9 at % Al) at a fixed detector position $2\theta = 15.8°$; i.e., almost in directions parallel to the [110] and $[\bar{1}10]$ axes and perpendicular to the [002]-FCC vector. From the peak width in the ω-scan, the mean size of the fcc-phase regions is also estimated by ~5 nm. The diffraction patterns shown in Figs. 2b and 2c also indicate that the fcc cells are embedded in the bcc lattice in a very definite way. The ratio of the intensities of the (200)-FCC and (220)-FCC peaks in Figs. 1b–1d allows us to conclude that, of the three possible variants of the embedding of fcc cells in the bcc lattice, one is preferable: the [001]-FCC axis of the nanocrystal coincides with the [001] axis, the [100]-FCC axis is directed along the $[1\,\bar{1}0]$ axis, and the [010]-FCC axis is directed along the [110] axis of the bcc crystal.

Figure 3 shows the diffraction patterns measured upon scanning along the [110] direction in single crystals of α-iron and the alloy with 7 at % Al, in which the fcc phase is absent, and the alloy with 9 at % Al. The scattering intensity distribution was measured in the intervals between the Bragg peaks (000) and (110), (110) and (220), and (220) and (330) of the bcc lattices. The diffraction pattern of the iron crystal has no singularities, and, in the case of the Fe–Al alloy (7 at %), only the asymmetry of the (110) and (220) peaks is observed, due to the contribution of diffuse scattering, as shown in [8].

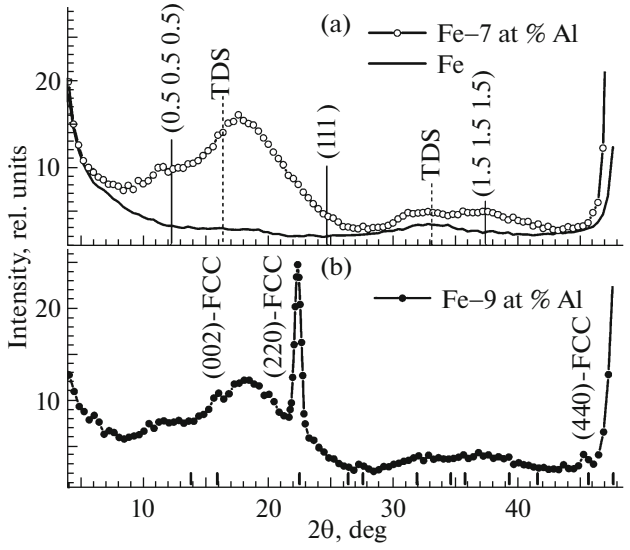

Fig. 5. Angular distribution of the scattering intensity upon scanning along the [111] axis of (a) an α-iron single crystal and (b) annealed single crystals of the iron–aluminum alloy samples containing (a) 7 and (b) 9 at % Al. The [111] axis lies in the plane of the alloy sample. Solid vertical lines show calculated position of superstructure peaks (0.5 0.5 0.5), (111), and (1.5 1.5 1.5); dashed lines—intersection of the scan path with the planes of thermal diffuse scattering (TDS); vertical strokes—position of the fcc-phase peaks.

The asymmetry of the left and right slopes at the (110) and (220) peaks is also seen in the diffraction pattern of the Fe–Al alloy with 9 at % Al, where two series of fcc peaks, (00*l*) and (*hhh*), are present. As described above, the contribution to peaks of the (00*l*) type is given by fcc nanocrystals whose two ⟨110⟩ axes coincide with the ⟨100⟩ axes of the bcc lattice. The presence of (*hhh*) peaks in the scan means that there is a third way, also with several variants of embedding, i.e., the orientations of the axes of the fcc cell relative to the axes of the bcc lattice. From Fig. 4a, where ω- and χ-scans through the maximum of the peak (222) at an angle 2θ = 27.4° in the diffraction pattern shown in Fig. 3b, one can see that the peak width is small. This means that fcc nanocrystals are embedded in the bcc lattice by this method quite unambiguously.

In a cubic cell, the angle between the vector [111] and vectors ⟨100⟩ is about 55°. Since the [111]-FCC axis coincides with the [110] axis of the bcc lattice, a variant is possible when one of the ⟨100⟩-FCC axes, with points of type {*h*00}, lies in the $(\bar{1}10)$ plane of the bcc crystal and deviates from the [001] axis of the bcc crystal by an angle of 35° = 90° – 55°. Indeed, a weak (200)-FCC peak is present in the χ-scan (at 2θ = 15.8°) shown in Fig. 4c. The trajectory of the scan (circular arc) lies in the $(\bar{1}10)$ plane of the bcc lattice. At χ = 36°, it intersects the [111] axis of the bcc lattice, where a wide diffuse peak is visible; at χ = 55°, it passes through the (200)-FCC site and, at χ = 90°, it crosses the [001] axis of the bcc lattice at the (200)-FCC point, but the contribution to it is given by nanocrystals whose axes are directed according to the second way of their embedding to the lattice of the bcc crystal.

The diffraction patterns from single crystals of α-iron and Fe–Al alloys, measured upon scanning along the [111] axis, which lies in the sample plane, are shown in Fig. 5. While, in the diffraction pattern of pure iron, only the contribution of diffuse scattering due to collective thermal vibrations of atoms (thermal diffuse scattering, TDS) is visible, in the diffraction patterns of the alloys, it overlaps with wide diffuse peaks (0.5 0.5 0.5) and (1.5 1.5 1.5) from regions with ordering of types $D0_3$ and (111) from regions with local *B*2 and $D0_3$-type ordering [8].

A contribution to the diffuse peak to the left of mark (111) is given not only by the $D0_3$ region, but also the regions with local *B*2-type ordering, which was thoroughly described earlier in [8] for the Fe–Al alloy (7 at % Al). Besides these diffuse peaks, the diffraction pattern of the Fe–Al alloy (9 at % Al), shown in Fig. 5b, has peaks of the fcc phase: strong (220)-FCC and weak (440)-FCC peaks. The presence of {*hh*0}-FCC points on the [111] axis of the bcc crystal is consistent with the third way of embedding, in which the ⟨111⟩-FCC axis coincides with the ⟨110⟩ axis of the bcc lattice. At the same time, the absence of {*hhh*}-FCC peaks means that the first way of embedding, in which the ⟨*h*00⟩-FCC axes coincide with the ⟨*h*00⟩ axes of the bcc lattice, is not realized. Thus, from the set of θ–2θ scans along the bcc axes [100] in Fig. 1, [110] in Fig. 3, and [111] in Fig. 5, we can conclude that, of the aforementioned three ways of the embedding of fcc cells in a bcc lattice, only the second and third are realized. In the second way, when two ⟨*h*00⟩-FCC axes are directed along the ⟨*hh*0⟩ axes of the bcc lattice and the third coincides with ⟨00*l*⟩ axis of the bcc lattice, three variants of embedding are possible (formally, 24, due to cubic symmetry). In the third way, when the ⟨*hhh*⟩-FCC axis coincides with the ⟨*hh*0⟩ axis of the bcc lattice and the ⟨*h*00⟩-FCC axis lies in the $\{\bar{1}10\}$ plane of the lattice of the bcc crystal, 12 variants of embedding are possible (formally, 24 variants, due to cubic symmetry).

In the Fe–Al (9 at % Al) and Fe–Ga (18 at % Ga) alloys, the parameter of the bcc lattice is approximately the same, ~0.29 nm. The alloys have nearly the same linear dependence of the parameter of the unit bcc cell on the concentration of the alloying element [11, 12]. Probably, for this reason, a new fcc phase also arises in the Fe–Ga alloy [9]. The diffraction patterns of samples of this alloy, measured upon θ–2θ scanning along the axes [001], [111], [110], and [221], are shown in Fig. 6. The Bragg bcc reflexes (002), (222), (110), and (220) are approximately four orders of magnitude stronger than the diffuse scattering observed between the (000) site and the first bcc peak and

between the bcc peaks themselves. As shown in [9], the contribution to it is due to scattering by $B2$-phase clusters, regions with a short-range order of the $D0_3$ type (long-range order appears after annealing), as well as thermal diffuse scattering (TDS is marked by vertical lines). In the case of a quenched sample, $D0_3$ peaks and peaks from the fcc phase are weakly evident, but, after annealing, as can be seen from Fig. 6, the intensity of $D0_3$ reflections increases by 1–2 orders of magnitude, and the fcc peaks are more pronounced.

Above, for the Fe–Al alloy (9 at % Al), we described three ways of embedding an fcc cell in a bcc cell, of which only two are mostly realized. It is important that in the case of the Fe–Ga alloy, the diffraction patterns shown in Fig. 6 have {00l}-FCC peaks measured upon scanning along the [001] axis; {hh0}-FCC peaks measured upon scanning along the [110] axis; the (442)-FCC peak measured upon scanning along the [221] axis and, in addition to the (400)-FCC peak at $2\theta = 31.7°$, {hhh}-FCC peaks measured upon scanning along [111] axis. Hence, in the Fe–18 at % Ga alloy, the first way of embedding is dominantly realized, when the axes of the fcc cells and the bcc lattice coincide, which is not observed in the case of the Fe–Al alloy.

It should be noted once again that, in Fig. 9 of [11], the diffraction pattern for a single crystal of the Fe–18.7 at % Ga alloy measured upon scanning along [HHH] axis has the expected superstructure peaks (0.5 0.5 0.5), (111), and (1.5 1.5 1.5) from the $D0_3$-phase regions. Their intensity increases significantly with increasing Ga concentration and strongly depends on the heat treatment conditions. After slow cooling of the sample, two additional peaks appear: the first is at $H_1 \sim 0.64$ and the second is at $H_2 \sim 1.28$. However the authors of [11] did not comment their appearence. The positions of these peaks agrees very well with those calculated for the (200)-FCC and (400)-FCC peaks, respectively, from the new fcc phase that we discovered, with a cell parameter of ~0.52 nm.

A comparison of the intensities of the peaks given in [11] shows that the peak at $H_1 \sim 0.64$, which, as can be assumed, is the (200)-FCC peak, is an order of magnitude weaker than the peak at $H_2 \sim 1.28$, which is supposedly the (400)-FCC peak. Then, it is natural that, in the diffraction pattern shown in Fig. 6b, the (200)-FCC is not seen. The presence of {h00} peaks in the diffraction pattern measured upon scanning along the [111] axis means that there is also a fourth way of embedding the fcc cell in the bcc crystal lattice. The available data are not enough to describe it, but this is not of fundamental importance at the moment. The important fact is that there are several ways of embedding of fcc nanocrystals in the bcc lattice of the alloy. At least, it is clear that the simple variant in which the ⟨100⟩ axis of the fcc cell coincides with the ⟨110⟩ axis of the bcc lattice, as can be seen from Fig. 6c, is not realized.

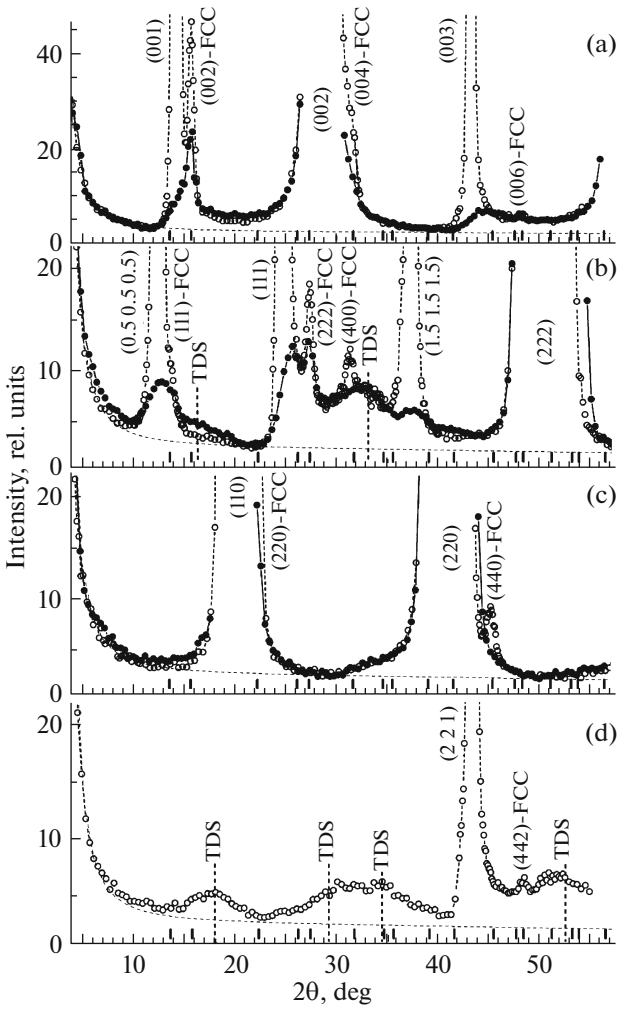

Fig. 6. Diffraction patterns of (filled circles) quenched and (empty circles) annealed Fe–Ga alloy samples obtained upon scanning along the directions (a) [001], (b) [111], (c) [110], and (d) [221]. The experimental error is approximately equal to the size of the character. The dashed line was obtained from the least-squares approximation of the minimum experimental points in diffraction patterns (background). Vertical strokes indicate the positions of the allowed peaks of the fcc phase.

Figure 7a shows the diffraction patterns measured upon ω-scanning through the maximum of the (002)-FCC peak, which is present in the diffraction patterns in Fig. 6a for both quenched and annealed samples of the Fe–Ga alloy. After annealing in the ferromagnetic state, the peak becomes narrower and its intensity at maximum increases, as it also occurs for superstructure $D0_3$ peaks [9]. A similar ω-scan through the maximum of the (222)-FCC peak, which is visible in Fig. 6b in the diffraction pattern of a sample subjected to annealing in the ferromagnetic state, is shown in Fig. 7b.

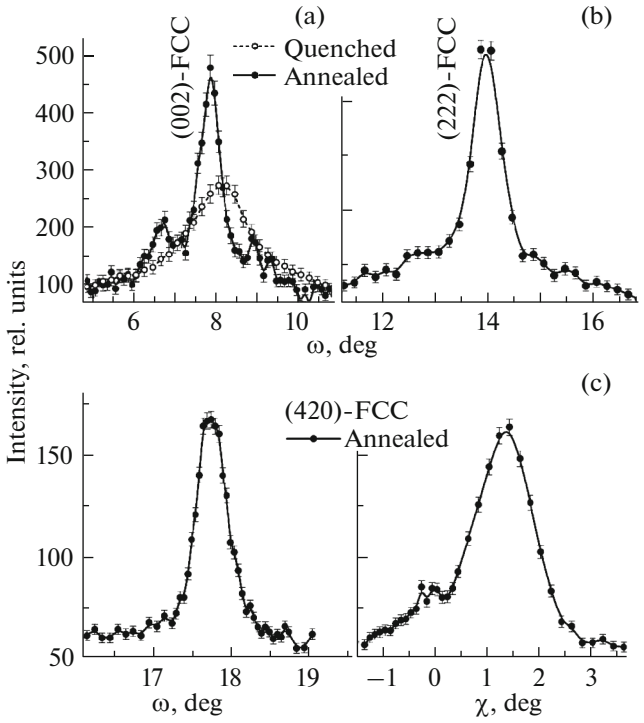

Fig. 7. Angular distribution of scattering intensity upon ω-scanning through the maxima of the peaks: (a) (002)-FCC shown in Fig. 6a for quenched and annealed Fe–Ga alloy samples, and (b) (222)-FCC shown in Fig. 6b for an annealed Fe–Ga alloy sample; (c) the same upon ω- and χ-scanning through the maximum of the (420)-FCC peak for the annealed Fe–Ga alloy sample.

Figure 7c shows the peak profiles measured upon ω- and χ-scanning through the maximum of the (420)-FCC peak of a Fe–Ga alloy sample subjected to annealing in the ferromagnetic state. The profiles of the (002)-FCC, (222)-FCC, and (420)-FCC peaks shown in Fig. 7, indicate that the fcc cell is embedded in the bcc lattice of the Fe–Ga crystal in a definite way. From the peak widths in the ω-scans, the mean size of the fcc-phase regions was estimated by ~7 nm. Since the integral intensity of the fcc phase of peaks is several orders of magnitude lower than that of the bcc peaks, the volume fraction of the new phase in the alloy both after quenching and after annealing is insignificant. It can be assumed that the appearance of the fcc phase in the Fe–Al alloy has some effect on the reduction in magnetocrystalline anisotropy, which begins just at an aluminum concentration of ~9 at %. However, finding out how significant the role of the new fcc phase is in the formation of the magnetic properties of Fe–Al and Fe–Ga alloys requires further studies.

4. CONCLUSIONS

On a four-circle X-ray diffractometer in the transmission geometry, the local ordering in single crystals of Fe–7 at % Al, Fe–9 at % Al, and Fe–18 at % Ga alloys was studied. One sample of each alloy was annealed in the ferromagnetic state, and another (Fe–18 at % Ga) was quenched in water after annealing in the paramagnetic state.

In addition to the phases previously observed in these alloys, i.e., regions of local ordering with a $B2$- and $D0_3$-type structure with sizes of ~0.6 nm in quenched samples and, several nanometers, in the annealed $D0_3$ samples, a new phase has been found. The type of local ordering in it is $B1$ (fcc, prototype NaCl), the lattice parameter is ~0.52 nm, and the mean size after annealing is 5–7 nm.

For the studied alloys from the set of scans along the ⟨100⟩, ⟨110⟩, and ⟨111⟩ axes of the bcc lattice, the following facts have been established. In the Fe–7 at % Al alloy, no local $B1$-type ordering is observed. It appears in the Fe–9 at % Al alloy, but, in this case, the axes of the unit cells of the nanocrystals—fcc-phase regions in a single crystal of the alloy—can be oriented with respect to the axes of the bcc lattice; i.e., an fcc cell can be embedded in the bcc cell in two ways, each allowing several variants. In the case of the Fe–18 at % Ga alloy, $B1$-type ordering is observed both in the quenched and annealed samples, but the volume of the fcc phase in the annealed sample is approximately twice as large as in the quenched one. There are also two ways with several variants of embedding an fcc cell in a bcc cell; they are different from those realized in the Fe–9 at % Al alloy. The existence of the new fcc phase discovered here is confirmed by the results of [11], where, among others, a single crystal of the Fe–18.7 at % Ga alloy was studied. However, the authors of [11] made no attempt to identify the superstructure peaks in X-ray diffraction patterns and ignored their presence.

FUNDING

This work was carried out as part of the state task "Magnet" no. AAAA-A18-118020290129-5 and project no. 8-10-2-5 of the Program of the Ural Branch of the Russian Academy of Sciences and was supported by the Russian Foundation for Basic Research (grant no. 18-02-00391).

CONFLICT OF INTEREST

The authors declare that they have no conflicts of interest.

REFERENCES

1. A. S. Freitas, D. F. de Albuquerque, I. P. Fittipaldi, and N. O. Moreno, J. Magn. Magn. Mater. **362**, 226 (2014). https://doi.org/10.1016/j.JMMM2014.03.055
2. J. R. Cullen, A. E. Clark, M. Wun-Fogle, J. B. Restor, and T. A. Lograsso, J. Magn. Magn. Mater. **226–230**, 948 (2001). https://doi.org/10.1016/S0304-8853(00)00612-0

3. U. R. Kattner and B. P. Burton, in *Desk Handbook: Phase Diagrams for Binary Alloys*, 2nd ed., Ed. by H. Okamoto (ASM Int., Materials Park, OH, 1993), p. 12. http://www.asminternational.org/documents/10192/1850140/57751G_Frontmatter.pdf/c36eeb4ed6ec-4804-b319-e5b0600ea65d.
4. O. Ikeda, R. Kainuma, I. Ohnuma, K. Fukamichi, and K. Ishida, J. Alloys Compd. **347**, 198 (2002). https://doi.org/10.1016/S0925-8388(02)00791-0
5. Yu. P. Chernenkov, N. V. Ershov, V. A. Lukshina, V. I. Fedorov, and B. K. Sokolov, Phys. B (Amsterdam, Neth.) **396**, 220 (2007). https://doi.org/10.1016/j.physb.2007.04.008
6. N. V. Ershov, Yu. P. Chernenkov, V. A. Lukshina, and V. I. Fedorov, Phys. Solid State **51**, 441 (2009). https://doi.org/10.1134/S1063783409030019
7. N. V. Ershov, Yu. P. Chernenkov, V. A. Lukshina, and V. I. Fedorov, Phys. Solid State **54**, 1935 (2012). https://doi.org/10.1134/S1063783412090107
8. N. V. Ershov, Yu. P. Chernenkov, V. A. Lukshina, and O. P. Smirnov, Phys. Solid State **60**, 1661 (2018).
9. Yu. P. Chernenkov, N. V. Ershov, and V. A. Lukshina, Phys. Solid State **60**, 2370 (2018). https://doi.org/10.21883/FTT.2019.01.46889.174
10. H. Basumatary, M. Palit, J. Arout Chelvane, S. Pandian, M. Manivel Raja, and V. Chandrasekaran, Scr. Mater. **59**, 878 (2008). https://doi.org/10.1016/j.scriptamat.2008.06.034
11. Y. Du, M. Huang, S. Chang, D. L. Schlage, T. A. Lograsso, and R. J. McQueeney, Phys. Rev. B **81**, 054432 (2010). https://doi.org/10.1103/PhysRevB.81.054432
12. Yu. P. Chernenkov, V. I. Fedorov, V. A. Lukshina, B. K. Sokolov, and N. V. Ershov, Phys. Met. Metallogr. **100**, 235 (2005).
13. *International Tables for Crystallography*, Vol. A: *Space-Group Symmetry*, Ed. by T. Hahn, 5th ed. (Springer, Dordrecht, The Netherlands, 2005), p. 911. http://chembaby.com/wp-content/uploads/2019/02/Hann-Theo-International-Tables-For-Crystallography.-Volume-A.-Space-group-Symmetry.pdf.
14. O. Kubaschewski, *Phase Diagrams of Binary Fe-based Systems* (Springer, Stahleisen, Berlin, Heidelberg, Düsseldorf, 1982), p. 135. https://www.springer.com/gp/book/9783662080269.
15. G. Bertotti and F. Fiorillo, in *Magnetic Alloys for Technical Applications. Soft Magnetic Alloys, Invar and Elinvar Alloys*, Ed. by H. P. J. Wijn (Springer, Berlin, 1994), p. 35. https://link.springer.com/chapter/10.1007/1006502817.
16. C. J. Quinn, P. J. Grundy, and N. J. Mellors, J. Magn. Magn. Mater. **361**, 74 (2014). https://doi.org/10.1016/j.JMMM.2014.02.004
17. B. E. Warren, *X-Ray Diffraction* (Dover, New York, 1990). https://www.amazon.com/s?k=0486663175&ref=nb_sb_noss.

Translated by E. Chernokozhin